Parameterization of the effects of vertically propagating gravity waves for thermosphere general circulation models: Sensitivity study

Erdal Yiğit,[1] Alan D. Aylward,[1] and Alexander S. Medvedev[2]

[1] A parameterization of gravity wave (GW) drag, suitable for implementation into general circulation models (GCMs) extending into the thermosphere is presented. Unlike existing schemes, the parameterization systematically accounts for wave dissipation in the upper atmosphere due to molecular viscosity, thermal conduction, ion friction, and radiative damping in the form of the Newtonian cooling. This is in addition to using the commonly employed breaking/saturation schemes, based on either linear Hodges-Lindzen instability criteria or its nonlinear extension to multiple-harmonic spectra. The scheme was evaluated in a series of tests of increasing complexity. In the thermosphere, the simulations suggest that the dissipation competes with the instability caused by amplitude growth, and can seriously alter GW propagation and the associated wave drag. Above the mesopause the GW drag is generally created by harmonics with fast horizontal phase velocities, which under favorable conditions can propagate into the F_2 layer. The effects of thermospheric dissipation are more complex than a simple exponential decay of GW fluxes above certain levels. We examine the sensitivity of the GW drag profiles to the variations of the source spectra typically employed in GCMs. These results suggest that GWs can provide strong coupling between the meteorological events in the lower atmosphere and the circulation well above the middle atmosphere.

1. Introduction

[2] Internal gravity waves (GWs) generated in the lower atmosphere play a crucial role in the modification of the energy and momentum budget of the mesosphere and lower thermosphere (MLT). Their effects are well understood in the middle atmosphere. GWs are responsible for the reversal of the mean zonal wind and the associated reversal of the meridional temperature gradient, turbulent mixing of chemical constituents and the transport of heat [*Fritts and Alexander*, 2003]. GWs interact with other type of waves of larger scale and modify their vertical propagation characteristics [*Williams et al.*, 1999]. There is increasing observational and modeling evidence that GWs are capable of significantly perturbing the upper atmosphere as well [*Oliver et al.*, 1997; *Kazimirovsky et al.*, 2003; *Djuth et al.*, 2004; *Miyoshi and Fujiwara*, 2008]. While the observational properties of GWs in the upper atmosphere have been extensively studied, there is still a lack of understanding of consequences in the thermosphere of GWs originating in the lower atmosphere. Since existing general circulation models (GCMs) do not resolve subgrid-scale waves, so-called GW (or GW drag) parameterizations are commonly used. This paper addresses the issue of how to properly account for GW effects in thermosphere models.

[3] Depending on their characteristics, vertically propagating GWs are able to penetrate into the thermosphere-ionosphere (TI), and deposit momentum and heat into the larger-scale flow. By contrast to the middle atmosphere, GW propagation into the TI is strongly influenced by molecular viscosity and thermal conduction [*Vadas and Fritts*, 2005], by ion friction, and to a lesser degree, by radiative damping, usually approximated in parameterizations by Newtonian cooling. In order to distinguish these dissipative mechanisms from the breaking/saturation caused by pure "internal" nonlinear effects associated with the instabilities at large amplitudes, we shall sometimes refer to the additional GW damping in the thermosphere as an "external" dissipation. Mathematically, the vertical attenuation of GW harmonics affected by dissipation is described by the imaginary part m^I of the vertical wave number $m = m^R - im^I$. The expressions for m^I have been found for molecular viscosity and heat conduction [*Vadas and Fritts*, 2005], ion friction [*Gossard and Hooke*, 1975], and Newtonian cooling [*Holton*, 1982]. Parameterizations of the GW momentum deposition and heating usually require a knowledge of the vertical flux of the horizontal eddy momentum (per unit mass) $F = \overline{u'w'}$, where the bar denotes an appropriate averaging. For harmon-

[1]Department of Physics and Astronomy, University College London, London, UK.
[2]Max Planck Institute for Solar System Research, Katlenburg-Lindau, Germany.

ics $(u', w') \sim (\hat{u}, \hat{w})\exp(-imz)$, the stress $\overline{u'w'} = \mathrm{Re}\ (\hat{u}\hat{w}^*)$, where $\hat{w}^*$ is the complex conjugated quantity, and, hence, the flux $F \sim \exp(-2m^iz)$.

[4] Since the early work of *Lindzen* [1981], a number of GW drag parameterizations have been developed [*Matsuno*, 1982; *Holton*, 1982; *Fritts and Lu*, 1993; *Medvedev and Klaassen*, 1995; *Hines*, 1997; *Alexander and Dunkerton*, 1999; *Meyer*, 1999a; *Warner and McIntyre*, 2001]. One of the first parameterizations of GW drag produced by waves affected by dissipation was proposed by *Matsuno* [1982]. Most of these schemes either do not treat GW propagation into the thermosphere, or apply ad hoc nonphysical techniques in order to represent wave dissipation above the MLT. For instance, the scheme of *Alexander and Dunkerton* [1999] considers only noninteracting and conservatively propagating GWs which deposit all their momenta at the level of convective instability determined by the *Lindzen* [1981] criterion. As a result, the drag profiles can be very noisy unless a large number of harmonics is used. An intermittency factor is required because the created drag values are too large. On the basis of the work by *Lindzen* [1981] and *Matsuno* [1982], *Meyer* [1999a] took into account only the molecular and eddy viscosity, and allowed multiple breaking levels.

[5] Recently, some GW parameterizations have been implemented into GCMs extending well into the thermosphere. Most of these models cover a vertical range from the surface up to ∼200–500 km. GW dissipation and propagation in the thermosphere have been treated in different ways. For instance, GW drag, heating and diffusion from *Hines* [1997] are exponentially damped to zero above 105 km in the Extended Canadian Middle Atmosphere Model (ECMAM) [*Fomichev et al.*, 2002]. In the Whole Atmosphere Community Climate Model-3 (WACCM3), *Garcia et al.* [2007] have incorporated the effects of molecular diffusion and radiative cooling (that are effective from 75 km to the model top at 145 km) into a Lindzen-type GW scheme. The Hamburg Model for the Neutral and Ionized Atmosphere (HAMMONIA) [*Schmidt et al.*, 2006] employs the *Hines* [1997] scheme that does not account for realistic GW dissipation in the thermosphere. The GCM at Kyushu University utilizes only an orographic GW scheme [*Miyoshi and Fujiwara*, 2008]. In the implementation of the *Hines* [1997] GW scheme into the Spectral Mesosphere-Lower Thermosphere Model (SMLTM), *Akmaev* [2001] took into account a viscous criterion for elimination of the harmonics that supersede the instability criterion above a certain height.

[6] GW dissipation, propagation and characteristics in the upper atmosphere have been extensively studied in numerical simulations. Focusing on single GW modes in the altitude range from 150 km to 600 km, *Klostermeyer* [1972] found that thermal diffusivity and molecular viscosity are the dominant dissipative mechanisms in the thermosphere, while the effects of ion friction are strong near the F_2 layer height. Using ray theory, *Hickey and Cole* [1988] estimated the amount of vertical energy flux loss due to thermal diffusivity, molecular viscosity and ion drag. *Vadas and Fritts* [2005] studied theoretically the damping of high-frequency GWs by molecular viscosity and thermal diffusivity in the thermosphere. *Vadas* [2007] considered the effects of thermal diffusivity and molecular viscosity on GWs within the framework of a ray trace

model. These studies have revealed important GW characteristics in the upper atmosphere, but they did not focus on the consequences to the thermosphere of GWs propagating from the lower atmosphere.

[7] Although a number of authors have studied the propagation of GWs into the thermosphere, the dissipative effects of molecular viscosity and thermal conduction, ion friction, and radiative damping were not properly taken into account in existing GW parameterizations. Therefore, the vertical coupling between the lower atmosphere and the TI due to GWs of meteorological origin could not realistically be simulated by GCMs.

[8] We describe a spectral GW parameterization that extends into the thermosphere and systematically accounts for the realistic dissipation in addition to breaking and saturation. A series of sensitivity tests were conducted with single and multiple harmonic GW spectra to study GW penetration into the thermosphere. Section 2 describes the GW scheme. Section 3 discusses the inclusion of the dissipation mechanisms. A brief outline of the implementation is given in section 4. Sensitivity experiments for single and multiple harmonic spectra are presented and discussed in sections 5–9.

2. Vertical Evolution of the Gravity Wave Horizontal Momentum Flux

[9] As with many GW drag parameterizations meant for implementation in GCMs, we assume vertically propagating harmonics, and employ the steady wave approximation. Effectively, this implies that subgrid-scale GWs do not leave a column of the model grid, and that the resolved (background) fields are viewed as time-independent during a time step. Vertical propagation of secondary GWs resulting from GW breaking and/or dissipation in the MLT [*Vadas et al.*, 2003] is not represented in the framework of this column model.

[10] The vertical flux (per unit mass) of the horizontal momentum associated with a GW harmonic i, $\overline{u'w'}_i$, varies with height according to [*Gavrilov*, 1990; *Medvedev and Klaassen*, 1995; *Alexander and Dunkerton*, 1999; *Vadas and Fritts*, 2005]

$$\overline{u'w'}_i(z) = \overline{u'w'}_i(z_0)\rho(z_0)\rho^{-1}(z)\tau_i(z), \tag{1}$$

where z_0 is the reference (source) level, $\rho(z) = \rho(z_0)\exp[-(z-z_0)/H]$ is the background density, H is the scale height, and $\tau_i(z)$ is the transmissivity. The overline denotes an appropriate averaging (coarse graining). Usually, temporal and spatial averaging is assumed over scales larger than the wavelength and period of the given harmonic, or the phase averaging. Summation over all components i is implied for broad GW spectra. For conservative propagation $\tau = 1$, and no divergence of the flux $\rho(z)F = \rho(z)\ \overline{u'w'}_i(z)$ occurs. In the case of dissipative wave propagation, the transmissivity can be conveniently represented as

$$\tau_i(z) = \exp\left[-\int_{z_0}^{z}\sum_d \beta_d^i(z')dz'\right], \tag{2}$$

where the flux attenuation functions $\beta_d^i(z')$ are attributed to different dissipation mechanisms denoted by the index d.

The relevant parameterizations for β_d^i are discussed in more detail in section 3.

[11] The flux $\overline{u'w'}_i(z)$ for individual harmonics is uniquely related to the wave amplitude $|u_i'| \equiv \sqrt{\overline{u_i'^2}}$ through the polarization relations:

$$|u_i'|(z) = \left[\frac{|\overline{u'w'}_i(z)||N(z)|}{k_h|c_i - \bar{u}(z)|} \right]^{\frac{1}{2}},\qquad(3)$$

where k_h is the horizontal wave number, N is the Brunt-Väisälä (buoyancy) frequency, c_i is the observed phase speed, and $\bar{u}$ is the mean wind. An important generalization of the wave amplitude for broad GW spectra consisting of M harmonics, is the total root mean square horizontal wind variance $\sigma = M^{-1} \left(\sum_i^M \overline{u_i'^2} \right)^{1/2}$. Vertical profiles of this quantity will be presented for several launch spectra in section 9.

[12] Once the distribution of wave fluxes is specified at a certain source level z_0 and the dissipation is parameterized in terms of $\beta_d^i(z)$, equation (1) can be integrated upward to find the vertical profile of the flux $\overline{u'w'}_i(z)$. The forcing exerted by dissipating and/or breaking GWs on the mean flow is given by the divergence of the wave momentum flux F divided by the mean density,

$$a(z) = -\frac{1}{\rho}\frac{\partial \rho F(z)}{\partial z}.\qquad(4)$$

The total mean wind acceleration ("wave drag") produced by the spectrum of GWs can then be represented with the help of (1) and (2) as the sum of contributions from individual harmonics:

$$a(z) = \sum_i^M a_i(z) = \sum_i^M \sum_d \beta_d^i \overline{u'w'}_i(z).\qquad(5)$$

The total heating by GWs consists of the heating due to dissipating harmonics, E_i, and the differential heating/cooling due to the wave-induced heat flux, Q_i. According to Medvedev and Klaassen [2003] and Becker [2004], these quantities for individual harmonics can be calculated as

$$E_i = c_p^{-1} a_i(c_i - \bar{u}), \quad Q_i = \frac{H}{2\rho R}\frac{\partial}{\partial z}[\rho(c_i - \bar{u})a_i].\qquad(6)$$

In the above expressions, R is the gas constant, c_p is the specific heat at constant pressure, and the coefficient 2 in the denominator follows from the assumption that the wave Prandtl number is equal to unity. Again, the summation over i is implied for the spectrum of GWs.

3. Wave Dissipation

[13] In the middle atmosphere, the vertical propagation of GWs is mainly affected by the nonlinear effects that limit their exponential growth. All GW drag schemes employed in middle atmosphere GCMs necessarily include a parameterization of wave breaking/saturation. In the thermosphere, other dissipative mechanisms compete with the nonlinearity, and can no longer be neglected. These mech-

anisms include molecular viscosity, thermal conduction, and ion drag [Hines, 1960; Hines and Hooke, 1970; Pitteway and Hines, 1963; Rishbeth, 1979]. We discuss these effects in the subsections that follow from the point of view of their implementation in GW schemes. Since some GCMs include radiative damping in the form of Newtonian cooling, we also consider it here.

3.1. Hodges-Lindzen Breaking Scheme

[14] According to the closure hypothesis of Hodges [1967] and Lindzen [1981], the exponential growth of wave amplitudes with height as a consequence of the decreasing background density is damped by convective instability when the amplitude $|u_i'|$ exceeds the instability threshold at the so-called breaking level

$$|u_i'| \geq |c_i - \bar{u}|.\qquad(7)$$

Following this assumption, the developing turbulence limits the wave Richardson number. In the case of constant background wind and temperature, this limits the wave amplitude growth with height. This allows one to express the dissipative function β_{lin}^i in terms of the mean quantities and wave parameters,

$$\begin{aligned}\beta_{lin}^i &= 0 & |u_i'| &< |c_i - \bar{u}| \\ \beta_{lin}^i &= \frac{1}{H(z)} + \frac{3\bar{u}_z}{c_i - \bar{u}} + \frac{N_z}{N} & |u_i'| &\geq |c_i - \bar{u}|,\end{aligned}\qquad(8)$$

where the subscript z denotes a vertical derivative. The first term on the right-hand side of the second equation in (8) follows from the effect of density variation with height, the second term takes into account vertical variations of the mean wind, and the third term describes the mean temperature vertical dependence. In practical implementations, many GW schemes assume the existence of only one "breaking" level above which the saturated harmonic is removed from further consideration [Holton, 1982; Alexander and Dunkerton, 1999]. This can be true if the critical level, that filters out the wave, lies immediately above the "breaking" level. However, this, generally, is not the case, especially in the thermosphere. Therefore, in our implementation, we allow multiple saturation levels by evaluating β_{lin}^i given by (8) at every level. Since the propagation of any one GW harmonic is assumed to be independent of other harmonics in the spectrum, we shall designate the described approach as the "linear" breaking/saturation scheme.

3.2. Nonlinear Saturation

[15] The nonlinear treatment of vertically propagating GWs in accordance with the theory of the nonlinear diffusive damping of Weinstock [1976], suitable for practical parameterizations, was introduced by Weinstock [1990] and further developed by Medvedev and Klaassen [1995, 2000]. In this approach, individual waves are "aware" of the other harmonics in the spectrum, and interact with them. According to the theory, harmonics with shorter vertical wavelengths impinge on any given wave i and cause instabilities on scales shorter than the wavelength of the harmonic under consideration. When averaged over the scale of the wavelength, these effects act as a nonlinear

"wave-induced" diffusion acting upon the probe wave. Harmonics with wavelengths (and periods) longer than that of the given wave serve as an additional background and induce a "nonlinear" Doppler shift. *Medvedev and Klaassen* [1995, 2000] showed that the latter is important only in the vicinity of critical levels, and can be neglected in most practical applications of GW drag calculations.

[16] The nonlinear dissipation acting on a particular harmonic is given by *Medvedev and Klaassen* [1995, 2000]

$$\beta_{non}^i = \sqrt{2\pi} N \frac{1}{\sigma_i} \exp(-\alpha_i^2), \qquad (9)$$

where σ_i^2 is the wind variance produced by the waves with intrinsic phase speeds $(c_j-\bar{u})$ smaller than the reference intrinsic phase speed of the harmonic i, $\sigma_i = (\Sigma_j u_j'^2)^{1/2}$. In equation (9), α_i^2 can be viewed as a generalization of the Richardson number for spectra (to the accuracy of the coefficient 1/2),

$$\alpha_i^2 = \left(\sqrt{2}\sigma_i\right)^{-2} |c_i-\bar{u}|^2 = N^2 / \left(\sqrt{2} m_i^R \sigma_i\right)^2. \qquad (10)$$

It is seen that, unlike in the Hodges-Lindzen case, β_{non}^i is a continuous function of height, and grows with the increase of amplitudes of the harmonics in the spectrum. The relationship between the linear and the nonlinear saturation can be illustrated using the Froude number defined for monochromatic, Fr_m, and broad, Fr_s, spectra,

$$\begin{aligned} Fr_m &= \frac{|m_i^R u'|}{N} = \left|\frac{u'}{c_i-\bar{u}(z)}\right| \\ Fr_s &= \frac{|m_i^R \sigma_i|}{N} = \left|\frac{\sigma_i}{c_i-\bar{u}(z)}\right|, \end{aligned} \qquad (11)$$

where $m_i^R = N/(c_i-\bar{u})$ is the real part of the vertical wave number. Linear wave breaking/saturation for a monochromatic harmonic occurs when $Fr_m \geq 1$. This harmonic in the broad spectrum breaks when $Fr_s \rightarrow 1$. Since σ_i includes a contribution from at least one (self-interaction) or more harmonics (self-interaction and wave-wave interactions), it is generally larger than the amplitude of a single harmonic, i.e., $\sigma_i \geq u_i'$. Therefore, the overturning occurs at lower amplitudes for the harmonic that nonlinearly interacts within the spectrum. A gradual, although rapidly increasing, damping of a given wave by other harmonics in the spectrum takes place at amplitudes smaller than the linear breaking threshold $Fr_m = 1$.

3.3. Molecular Viscosity and Thermal Conduction

[17] The effects of molecular viscosity ν_{mol} and thermal conduction on GWs are negligible below about 80 km, but become increasingly significant in the thermosphere owing to their exponential growth. We adopt the parameterization for ν_{mol} after *Banks and Kockarts* [1973],

$$\nu_{mol} = 3.563 \times 10^{-7} T^{0.69}/\rho, \qquad (12)$$

where T is the background temperature. The molecular thermal conductivity κ, acts together with the molecular dissipation to attenuate the wave, and is related to ν_{mol} via the Prandtl number Pr,

$$\kappa = Pr^{-1}\nu_{mol}c_p. \qquad (13)$$

The corresponding dissipation term β_{mol}^i follows from the expressions for the imaginary parts of the vertical wave numbers [e.g., *Vadas and Fritts*, 2005, equations (41) and (47)]. For example,

$$\begin{aligned} \beta_{mol}^i(z) &= \frac{\nu_{mol}N^3}{k_h[c_i - \bar{u}(z)]^4} \quad (Pr = \infty) \\ \beta_{mol}^i(z) &= \frac{2\nu_{mol}N^3}{k_h[c_i - \bar{u}(z)]^4} \quad (Pr = 1). \end{aligned} \qquad (14)$$

[18] It is seen from (14) that the effects of molecular dissipation are scale-dependent. Harmonics with smaller vertical wavelength (smaller $|c_i-\bar{u}|$) dissipate faster, and the power -4 dependence is rather steep. This has important implications for the ability of fast GWs to penetrate higher into the thermosphere (see section 7).

3.4. Ion Drag

[19] "Ion friction" is a phenomenon caused by the effects of the ionized atmosphere on the neutral flow. It results from the relative motion of ions and neutrals in the TI. Charged particles and neutrals have different mobilities. Ions that are strongly controlled by the Earth's magnetic field exert a drag force on the neutral particles that are governed by gravity, pressure gradient and the Coriolis force. This drag is proportional to the difference between the neutral wind velocity $\mathbf{u}$ and the ion drift velocity $\mathbf{v}_i$, and to the effective collision frequency for momentum transfer between neutrals and ions ν_{ni} (neutral-ion collision frequency): $-\nu_{ni}(\mathbf{u}-\mathbf{v}_i)$. At F_2 layer heights, the ion friction significantly controls thermospheric winds, and can be as large as 1500 m s^{-1} d^{-1}. It has strong day-night variations.

[20] We adopt an approximation for ν_{ni} from *Klostermeyer* [1972], assuming that ν_{ni} is proportional to the ion number density n_i as follows:

$$\nu_{ni} = 7.22 \times 10^{-17} T^{0.37} n_i. \qquad (15)$$

Even in the presence of large electric polarization charges, the difference between the total electron and ion number densities is small [*Johnson and Hulbert*, 1950]. Therefore, we make an assumption of electrical neutrality, i.e., that the number density of charged particles is equal to the electron number density n_e and is the sum of all positive ions n_i^+, i.e., $n = n_e = \Sigma_j n_{ij}^+$.

[21] The expression for the imaginary part of the vertical wave number for GWs affected by ion drag is given, for example, by the formula (48–19) of *Gossard and Hooke* [1975]. Its rigorous application to defining the vertical damping rate β_{ion}^i, would require a knowledge of the respective directions of the wave vector and the magnetic field of the

Background field characteristics
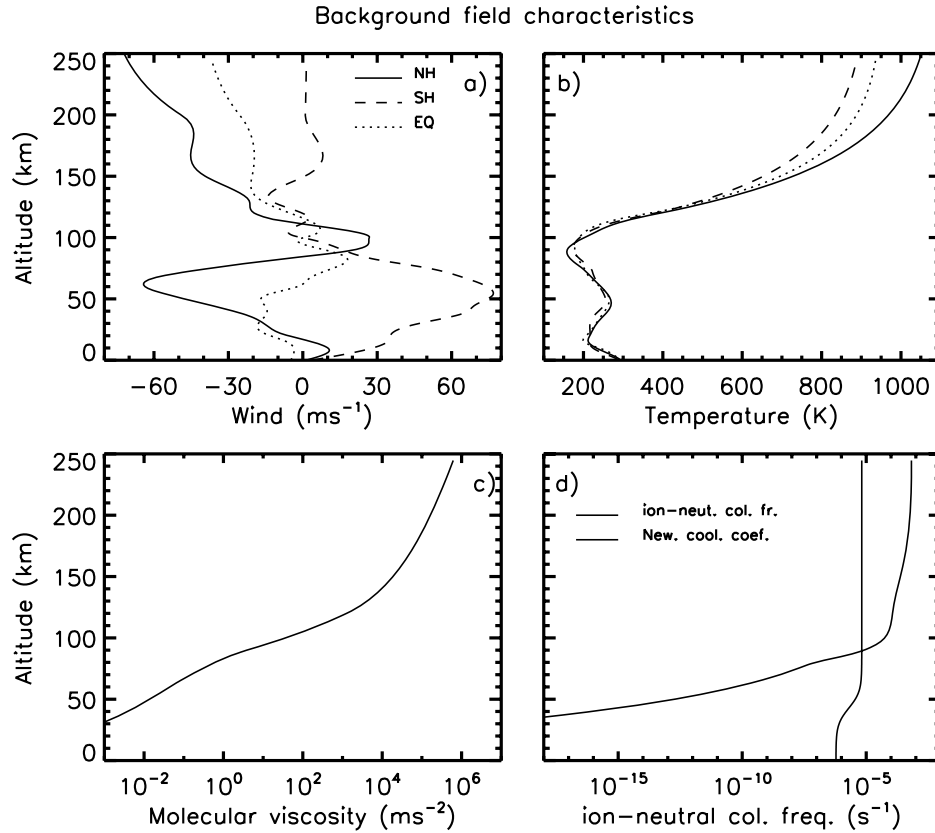
Figure 1. Vertical profiles of the background and dissipative parameters used in the calculations: (a) zonal wind and (b) temperature for 40°N, 40°S, and the equator in July. (c) The kinematic viscosity v_{mol} and (d) ion-neutral collision frequency v_{in}, and the Newtonian cooling coefficient α_{new} at 40°N.

Earth. However, the corresponding term is relatively small compared to the other terms of the expression, and we neglect it here. This yields

$$\beta^i_{ion} = \frac{2\nu_{ni}N}{k_h[c_i - \bar{u}(z)]^2}. \tag{16}$$

An example of the vertical profile of ν_{ni} for moderate solar and geomagnetic activity ($F_{10.7} = 140$, $Kp = 40$) in the Northern Hemisphere (NH) at 40° in July is plotted in Figure 1d. The temperature profile is taken from MSISE-90 [*Hedin*, 1991], and the n_e profile is from the CHIU model [*Chiu*, 1975]. In the real atmosphere, n_i depends on solar and geomagnetic activity, and is highly variable compared to molecular dissipation.

3.5. Newtonian Cooling

[22] Newtonian cooling is a proxy for the effects of radiative damping on the subgrid-scale GWs. The expression for Newtonian cooling is adopted from *Holton* [1982]. The associated damping rate is similar to equation (16), but with ν_{in} replaced by the Newtonian cooling coefficient α_{newt}. An example of the vertical profile of α_{newt} for the NH in July at 40° is shown in Figure 1d. It is important to note that these scale-dependent radiative damping coeffi-

cients are not accurate enough as they are, generally, functions of temperature and radiatively active species.

4. Outline of the Implementation and Sensitivity Tests

[23] Observed GW spectral characteristics are highly variable [*Allen and Vincent*, 1995; *Wu and Waters*, 1996; *Nakamura et al.*, 2001; *Espy et al.*, 2006]. The spatial and temporal variations of GW spectra (seasonal, geographical, diurnal, intraday, etc.) represent the biggest challenge for parameterizations in numerical modeling. Therefore, in this paper we adopt the typical Gaussian source spectrum [*Meyer*, 1999a, 1999b; *Alexander and Dunkerton*, 1999; *Garcia et al.*, 2007],

$$\overline{u'w'}_i(z_0) = \mathrm{sgn}(c_i - \bar{u}_0)\overline{u'w'}_{max} \exp\left[-(c_i - c_s)^2/c_w^2\right], \tag{17}$$

with the maximum of the flux $\overline{u'w'}_{max}$, set at $c_i = 0$, c_i being the phase velocity of the ith harmonic. The parameter c_w characterizes the half-width of the Gaussian momentum flux distribution, c_s gives the amount and direction of the $\overline{u'w'}_{max}$ shift, $\bar{u}_0$ is the lower boundary wind speed, and $|c_{max}|$ defines the fastest harmonics in the spectrum (in both directions). The latitudinal characteristics of the spectrum are determined by the source level wind $\bar{u}_0$. If $\bar{u}_0 = 0$, then

the spectrum is latitudinally invariant. If $|\bar{u}_0| > 0$, then the $\overline{u'w'}_i$-spectrum is shifted, depending on the direction of the source level wind.

[24] Once the phase velocities and the fluxes are prescribed at the source level for all harmonics in the spectrum, the fluxes are then evaluated step by step upward starting from the lowest level to the top of the model domain. Individual wave fluxes are computed from (1) taking into account the chosen dissipation decrements β_d^i, outlined in sections 3.1–3.5. Note that β_{lin}^i and β_{non}^i are used interchangeably. The corresponding wave amplitudes $|u'|$ are calculated from (3) for a chosen set of harmonics, and are used for finding the variance σ_i in (9). Finally, wave drag and heating rates are determined, as described in section 2.

[25] In the sensitivity experiments presented below, we investigate GW dynamics in a single column model in which a slow time dependence of the mean flow is implicitly excluded in the associated GW equations (the steady wave assumption). The background zonal mean zonal wind profiles were taken from the Horizontal Wind Model (HWM) [*Hedin et al.*, 1996], and the mean temperature profiles are from the MSISE-90 model [*Hedin*, 1991]. In order to evaluate ν_{ni}, the electron density data from the CHIU ionospheric model [*Ching and Chiu*, 1973; *Chiu*, 1975] were used. The standard test grid extends from 16 km to around 300 km with the vertical discretization of about one ninth of the altitude-dependent scale height.

5. Single Harmonic

[26] A GW spectrum consisting of a single harmonic represents the simplest possible scenario, which allows us to demonstrate the details of the wave propagation and attenuation in the TI. To remove the effects of critical line filtering from consideration, we assume zero background wind, $\bar{u} = 0$, but vertically varying temperature $\bar{T}(z)$ corresponding to a midlatitude summer (Figure 1b). Since dissipation strongly depends on the phase velocity, we present two runs with harmonics $c_1 = 60$ and $c_2 = 80$ m s^{-1}. The fluxes (per unit mass) at the source level are $\overline{u'w'}(z_0) = 3 \times 10^{-5}$ and 4×10^{-5} m^2 s^{-2}, correspondingly. They were normalized in such a way that the amplitudes $|u'_1|$ and $|u'_2|$ of the harmonics coincide at the launch level $z_0 = 16$ km. The horizontal wave number used in calculations is $k_h = 2\pi/200$ km^{-1}. We keep k_h constant throughout this study.

[27] Figures 2a, 2b, and 2c and 3a, 3b, and 3c present the wave drag a_i, wave amplitude $|u_i'|$, and the vertical damping rates β_d^i, correspondingly, computed for both harmonics with either β_{lin}^i or β_{non}^i and with the sum of the "external" dissipation turned off. In the case of a single harmonic, the nonlinear dissipation is the result of the wave interaction with itself. It is seen that the GW drag in the linear Lindzen-type scheme is much stronger than that using the nonlinear parameterization (note the logarithmic scale of the horizontal axis). This occurs because β_{lin}^i turns on instantaneously (Figures 2c and 3c) and at larger wave amplitudes (Figures 2b and 3b). In the nonlinear scheme, β_{non}^i is nonzero already at smaller amplitudes (and about 10–20 km lower in altitude), and increases gradually. It rapidly grows reaching its maximum about 10 km lower

than the level where the linear saturation switches on, and provides a strong amplitude decay. Above this altitude, β_{lin}^i and β_{non}^i have similar vertical profiles in the thermosphere, balance the wave amplitude growth, and provide height-independent momentum deposition. For the c_2 harmonic, the linear and nonlinear saturation levels are slightly shifted upward owing to the need for a larger wave amplitude to reach the instability threshold.

[28] Inclusion of Newtonian cooling (Figures 2 and 3, second row) modifies the effects of the linear or nonlinear saturation in the MLT, but has a small effect on the propagation of GWs into the thermosphere. Ion drag (Figures 2 and 3, third row) and molecular viscosity and thermal conduction (Figures 2 and 3, fourth row), limit wave amplitudes in the thermosphere much more. For example, ion drag limits $|u'_{60}|$ to 10 m s^{-1} at 170 km with the nonlinear damping scheme, and at 190 km with the linear one. In the calculation with molecular viscosity, these numbers reduce to 130 and 140 km, respectively. It is seen that β_{ion}^i, and especially β_{mol}^i, compete with β_{lin}^i or β_{non}^i (Figures 2 and 3, the third column): β_{mol}^{60} and β_{ion}^{60} dominate in the lower thermosphere, have a similar importance as β_{non}^{60} at around 120 km and, again, exceed β_{non}^{60} higher up. As a consequence, the wave drag no longer remains constant with height, but decays vertically. Inclusion of all dissipative processes reduces its peak value by a factor of about 4 to 5. It is important to note that the linear saturation criterion is not reached at all when ion drag and molecular viscosity are included. This occurs because in both simulations the wave amplitude is significantly damped by the external dissipation far below the convective instability threshold. Therefore, the dotted lines in Figures 2m and 3m show the drag profiles created by the total external dissipation only. Although they may appear to be close to the profiles calculated with β_{non}^i (solid lines), the difference is quite large, for example, ~300 m s^{-1}d^{-1} at 130 km for the harmonic c_2.

[29] Examination of the results plotted in Figures 2 and 3 shows that faster waves saturate higher since they require larger amplitudes, comparable with the phase velocities (as the intrinsic and phase velocities coincide for $\bar{u} = 0$). At the same time, faster waves are less affected by dissipation and can generally penetrate higher before being absorbed. Our results are in agreement with the analytic modeling work by *Vadas and Fritts* [2005], and general circulation modeling by *Miyoshi and Fujiwara* [2008]. They also demonstrated that large phase speed (large vertical wavelength) GWs dissipate higher in the atmosphere.

[30] The chances for the harmonic of reaching the linear breaking/saturation level are lower than of meeting the nonlinear saturation condition. The relative importances of various damping processes depend, among other parameters, on the phase velocity of the harmonic. For example, β_{non}^{60}, β_{mol}^{60}, and β_{ion}^{60} have the same values near ~115 km where the maximum of wave drag occurs (Figure 2o). The faster c_2 harmonic is less affected by molecular viscosity and ion drag, and thus its amplitude can further increase (Figures 2n and 3n). Consequently, the nonlinear saturation exceeds the "external" dissipation near the maximum of wave drag by a factor of about 5 (see Figure 3o and note the logarithmic axis scale).
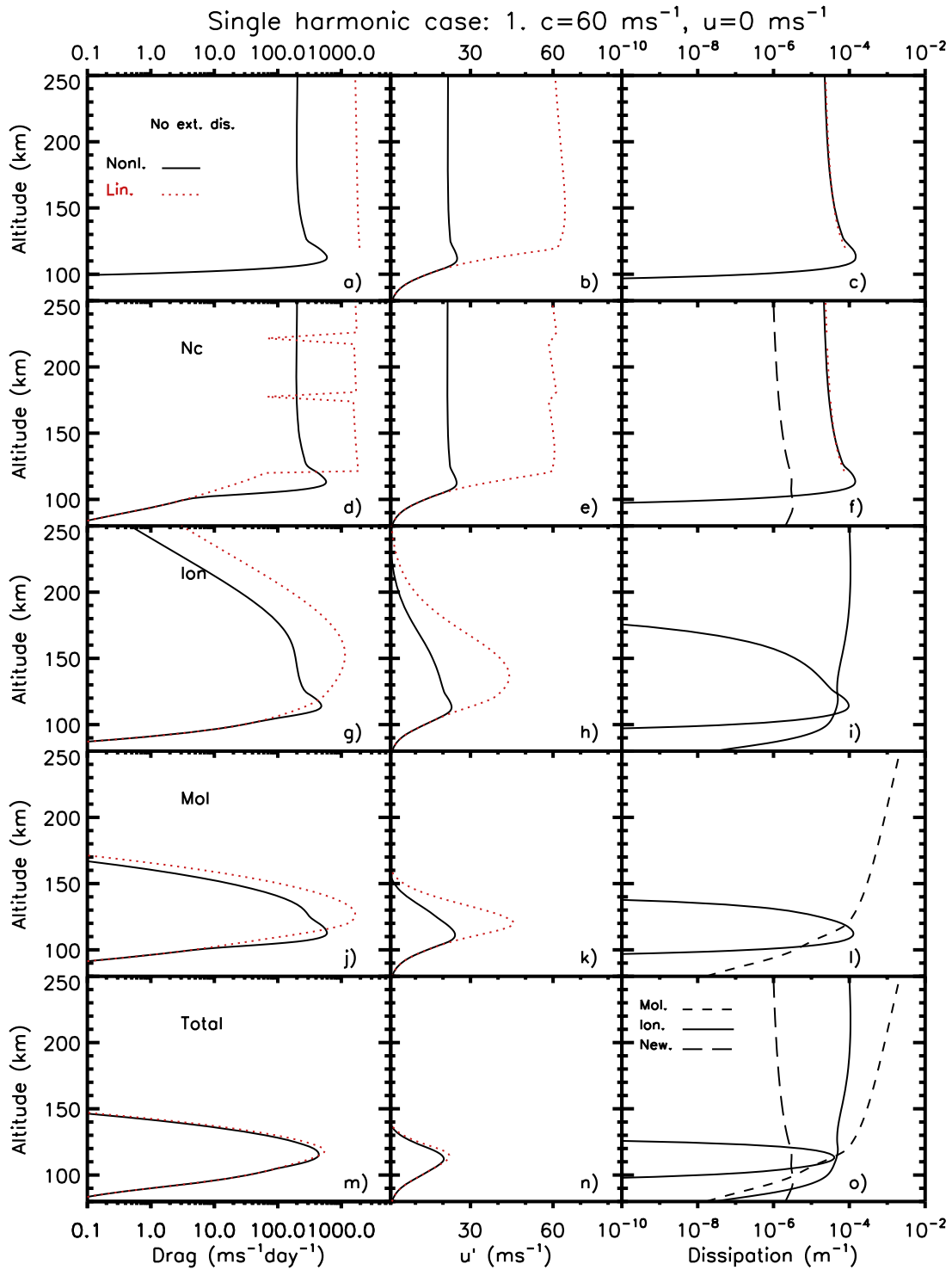
Figure 2. Single harmonic ($c = 60$ m s^{-1}, $\overline{u'w'}_i(z_0) = 3 \times 10^{-5}$m^{2}s^{-2}, RMS ≈ 0.018 m s^{-1}) tests in the windless atmosphere: (a–c) without external dissipation; (d–f) with β_{nc} only; (g–i) with β_{ion} only; (j–l) with β_{mol} only; and (m–o) including all dissipative terms. (left) The GW drag a_i, (middle) the wave amplitude u'_i, and (right) the vertical damping decrement β_d^i. The black solid and red dotted lines represent the nonlinear and linear schemes, respectively.

[31] The results of this section agree with the established fact that molecular viscosity and thermal conduction are the major contributors to GW damping in the thermosphere, with ion friction playing a secondary but important role. Although the exact profiles of GW drag depend on the combination of the source amplitude, phase velocity, and the vertical distribution of dissipative parameters, the highly idealized tests presented here demonstrate several clear
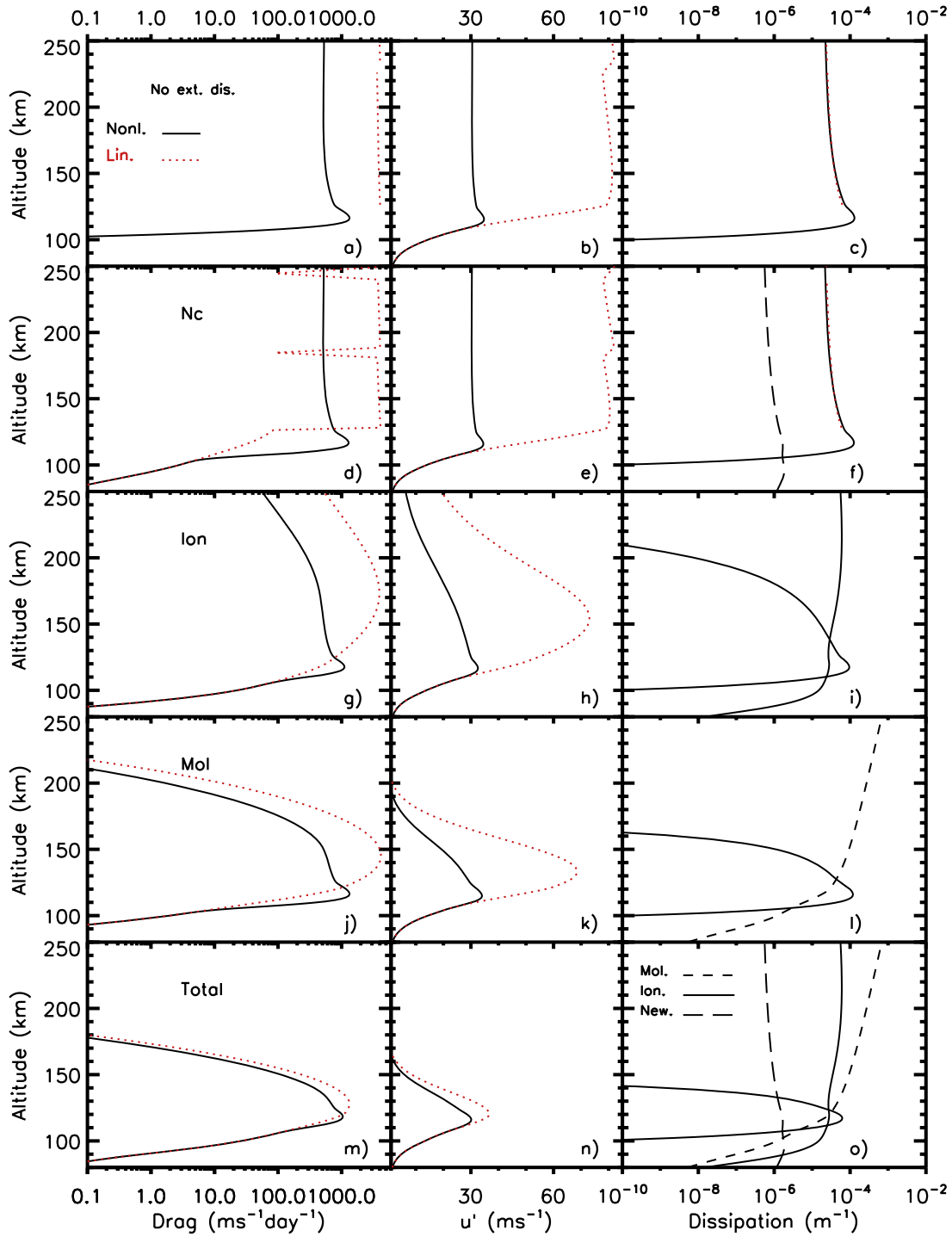
Figure 3. Same as in Figure 2, but for the harmonic with $c = 80$ m s^{-1}, $\overline{u'w'}_i(z_0) = 4 \times 10^{-5}$ m^2 s^{-2}, RMS ≈ 0.018 m s^{-1}.

conclusions. They are as follows. (1) Despite the strong damping, GWs can propagate well into the thermosphere and create noticeable momentum deposition. (2) The effects of the dissipation in the thermosphere compete with the breaking/saturation caused by instabilities of waves at large amplitudes. Therefore, both processes must be accounted

for in GW parameterizations. (3) The linear (convective) Hodges-Lindzen-type instability threshold may not be achieved by some harmonics in the thermosphere because of the significant attenuation by molecular viscosity and ion drag, while the very same harmonics can be affected

by the "nonlinear" dissipation due to the weaker breaking/saturation criteria.

6. Multiple Harmonic Spectrum in the Windless Atmosphere

[32] Having considered the propagation in the thermosphere of individual GW harmonics, we now make one stage more sophisticated experiments, and explore the effects of spectra consisting of multiple waves. As in the previous section, we again assume $\bar{u} = 0$ in order to eliminate the refraction and critical line filtering by the background wind. With the source spectrum (17) symmetric with respect to the phase velocity $c = 0$ and zero background wind, the drag produced by an individual wave is exactly canceled by that induced by the harmonic traveling in the opposite direction. Therefore, we use only a half of the spectrum (17) with $c > 0$ in the calculations presented in this section. To emphasize the role of faster GWs in the thermosphere, the calculations were performed for the spectra extending from +5 to +60 m s^{-1} (denoted as "Case 1") and from +5 to +80 m s^{-1} ("Case 2"). The calculations were repeated for M = 10, 20, and 200 harmonics to demonstrate the sensitivity of the results to the spectral resolution. In order to enable a proper comparison between the simulations, the amplitudes of individual harmonics were normalized by adjusting $\overline{u'w'}_{max}$ such that the total momentum flux (per unit mass) at the source level $F_{total} = \Sigma_i^M \overline{u'w'}_i$, is kept constant. The same spectral width $a_w = 30$ m s^{-1} was used in all the experiments in this section.

[33] The profiles of the calculated GW drag are represented in Figure 4 for Cases 1 and 2, by thin and thick lines, respectively. Figure 4 (left) shows the results obtained using only linear or nonlinear saturation, and Figure 4 (right) is for the tests including also external dissipation, i.e., $\beta_{tot} = \beta^i_{mol}{}^i + \beta^i_{ion}{}^i + \beta^i_{nc}$. There is an obvious difference between the results. The linear or nonlinear damping on its own balances the exponential growth of the wave amplitudes and yields a GW drag which is constant with height. Inclusion of external dissipation not only reduces the amplitude growth, but also destroys the waves altogether lower in the thermosphere, thus limiting the vertical extension of the associated GW drag. In the runs without external dissipation (marked as "No ext. dis."), the linear saturation mechanism produces increasingly large drag values when the number of harmonics increases. With M = 200 harmonics the associated drag exceeds 10^5 m s^{-1} d^{-1}. This occurs because the waves have smaller amplitudes at the source level, and therefore generally saturate independently higher up. The contributions from individual waves accumulate with the increase in number of participating harmonics. By contrast, the drag produced in the runs with the nonlinear β^i_{non} is smaller in magnitude, and does not change significantly when the number of harmonics grows. This happens because the saturation criterion in the nonlinear saturation relies on the overall characteristics of the spectrum, which does not depend on the spectral resolution. That is, it depends on the wind variance σ_i^2, produced by all harmonics with smaller than c_i phase velocities. The changes in the GW drag profiles computed with the nonlinear damping β^i_{non} for M = 10, 20, and 200 reflect only the numerical errors associated with spectral resolution. Since the resulting drag is generally smaller than that in the conventional Hodges-Lindzen linear saturation approach, no additional tuning parameters in the form of so-called "intermittency factors" are required.

[34] The GW drag in the middle atmosphere depends more on the spectral resolution than it does in the thermosphere for both runs with and without the external dissipation. For example, a drag of 1 m s^{-1}d^{-1} is observed 20–25 km lower in the middle atmosphere in the experiments with M = 200 compared to M = 10. This drag is created by the lower phase velocity portion of the spectrum, and the reduced spectral resolution yields an obvious effect. In the thermosphere, higher phase velocity harmonics of the broader spectrum in Case 2 (thicker lines) are responsible for the almost 20 km higher extension of the GW drag, to 160 km compared to 140 km in the runs with the external dissipation included. A smaller number of harmonics in the spectrum affects the decay of the GW drag little in all the experiments above 120 km. Although molecular viscosity and ion drag are weaker for the faster waves, the associated vertical damping rates (β_{tot}) are larger than with β^i_{non}. This is because nonlinear saturation occurs higher up when amplitudes approach the phase velocities. At these altitudes, molecular viscosity and ion friction already become important.

[35] The most dramatic difference between the linear and nonlinear saturation schemes is seen in the lower thermosphere. Despite the increasing effect of the total external dissipation, the drag in the runs with the linear saturation strongly depends on the number of harmonics M, and increases with it. Its values vary from 400 m s^{-1} d^{-1} to 10^4 m s^{-1} d^{-1} in the experiments with M = 10 and M = 200. Conversely, the nonlinear saturation scheme produces GW drag which is relatively independent of M. Having 20 times more harmonics changes the resulting drag only by a factor of around 2. The comparison of cases 1 and 2 shows that the peak drag values are quite similar. The main difference is above 120 km where the additional harmonics with $c_i > 60$ m s^{-1} change only the upper slopes of the drag profiles in the thermosphere.

[36] Overall, our sensitivity tests show that the linear Hodges-Lindzen-type saturation scheme provides an unrealistically high GW drag in the thermosphere. It inherently requires an "intermittency factor" to yield values typically known for the dynamical effects of GWs in the middle atmosphere and especially in the thermosphere [Fritts and Alexander, 2003]. Moreover, as our simulations confirm, this "intermittency factor" must be dependent on the spectral resolution. By contrast, the nonlinear saturation scheme is independent of the number of harmonics representing the GW spectrum, and yields more reasonable drag values and smoother vertical profiles. The high phase velocity portion of the spectrum, and systematically accounting for molecular viscosity and ion friction, critically shapes the wave drag profiles in the thermosphere.

7. Multiple Harmonic Spectrum in the Atmosphere With a Wind Shear

[37] Neglecting the presence of background wind provides limited insight into the behavior of GWs in the TI. A height varying wind profile affects both the generation and propagation of waves, thus significantly altering their impact on the flow in the thermosphere. We present sensitivity tests
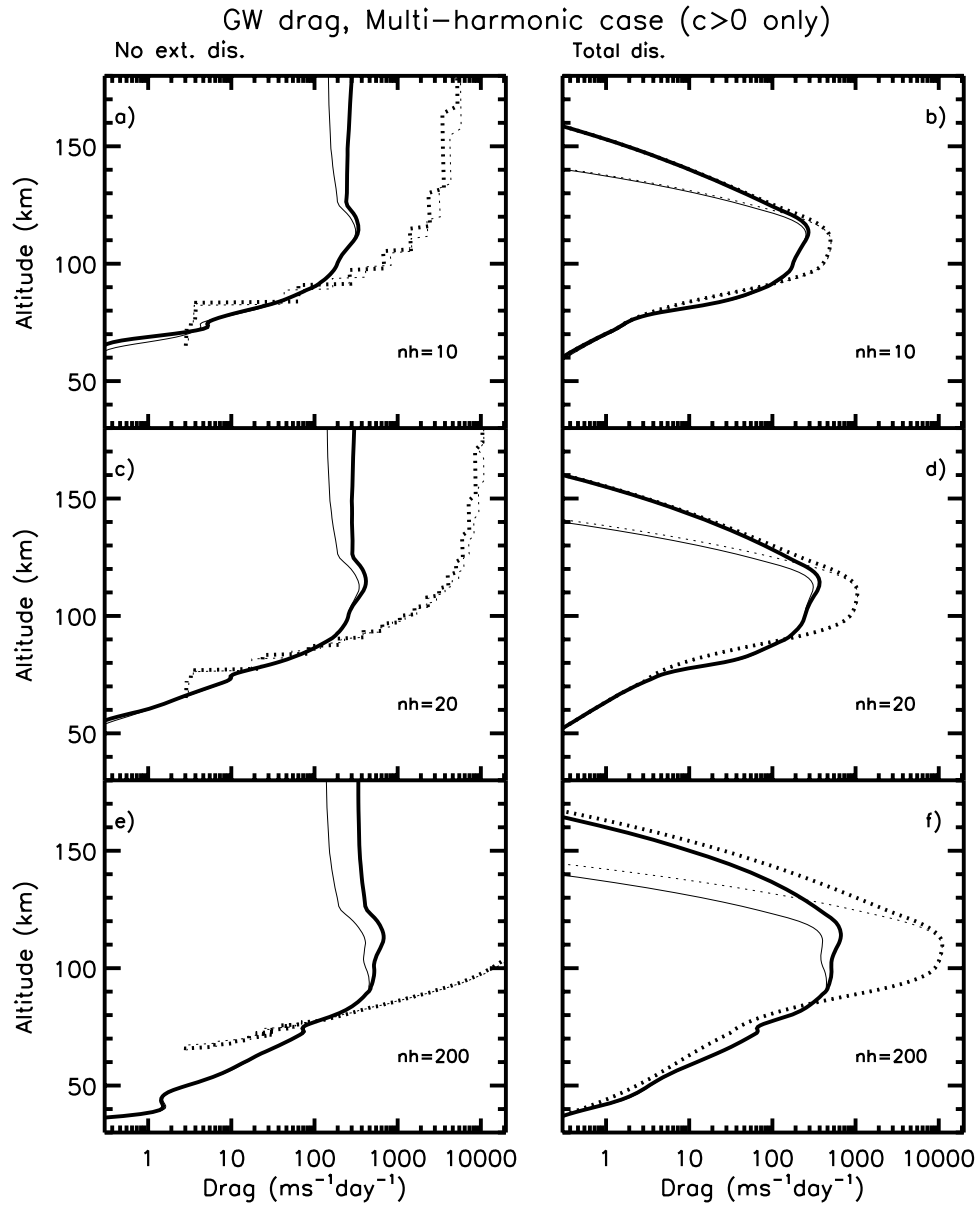
Figure 4. Multiharmonic simulations in the windless atmosphere: Vertical profiles of GW drag with nonlinear (solid line) and linear (dotted line) diffusive damping. Results with two different phase speed spectra with the normalized total momentum flux of 0.0008 m² s⁻² are overplotted. Thin lines denote "Case 1" extending from 5 to 60 m s⁻¹, and thick ones represent "Case 2" with 5 to 80 m s⁻¹. Shown are (top) 10, (middle) 20, and (bottom) 200 harmonics. Profiles (left) without "external" dissipation (No ext. dis.) and (right) with all dissipative factors included (Total dis.).

for three typical solstitial wind and temperature profiles shown in Figures 1a and 1b corresponding to the latitudes 40°N, 40°S and the equator in June (see section 4 for more details). These profiles exclude the variations due to diurnal and semidiurnal tides. In the middle atmosphere, they have large amplitudes and superimpose the zonal mean wind in a variety of combinations and phases. The HWM background wind used in this sensitivity study can be viewed as a partial case when tides are at certain phases. Thus, the resulted GW drag roughly corresponds to zonal mean quantities.

[38] The limited scope of this paper allows us to focus only on certain parameters which control the morphology of the source spectra (17). It is unlikely that this oversimplified

approximation for real sources fully represents the variety of GW spectra in the lower atmosphere. However, the shape and the range of parameters for the model spectra are similar to the ones used in GCMs. Here we discuss the sensitivity of the thermospheric response to the spectral shift c_s of the momentum flux $\overline{u'w'}_i(z_0)$, to the wind $\bar{u}_0$ at the source level, and to the spectral extent (the maximum phase speed c_{max}). In the calculations to be presented, we assume that the spectrum is equally spaced, i.e., $\Delta c = 2c_{max}/(M-1)$. In principle, a variable Δc similar to that of *Medvedev and Klaassen* [2000] can be used, too. As the results of the previous section suggest, the spectral resolution is relatively unimportant for the nonlinear saturation scheme with β^i_{non},
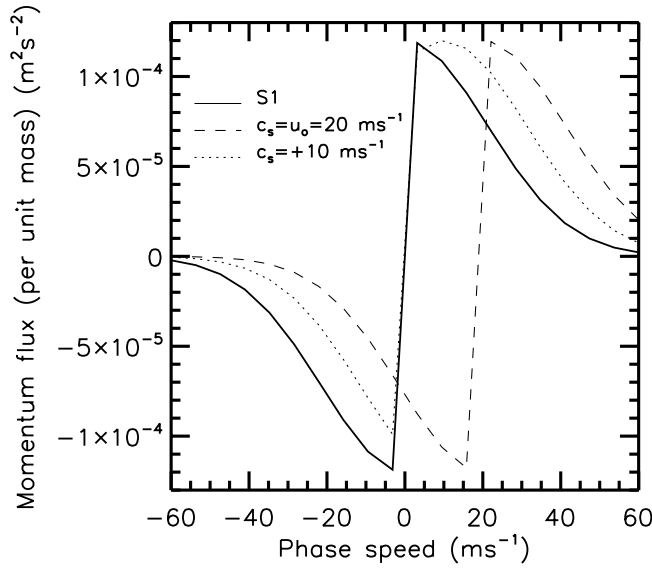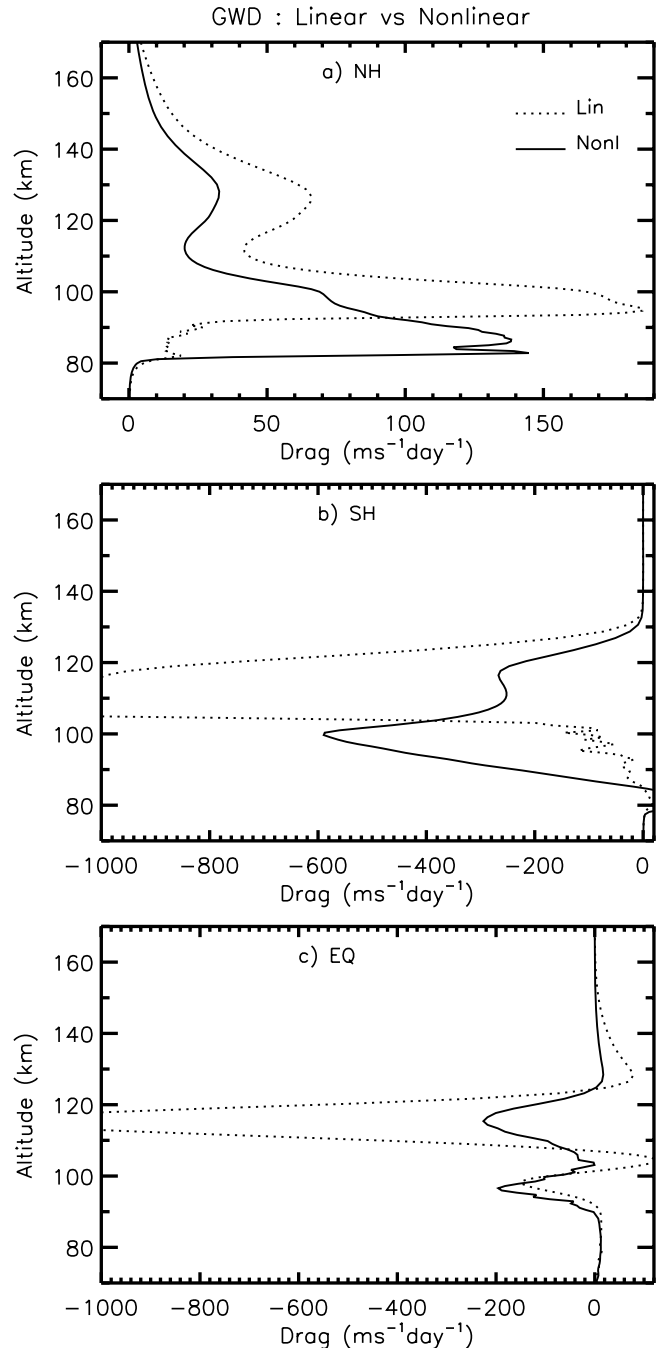
Figure 5. Momentum flux spectrum at the source level used in the calculations. The solid line denotes the S1 spectrum extending from -60 to $+60$ m s^{-1}, $\overline{u'w'}_{max} = 0.00012$ m^2 s^{-2}, $c_w = 45$ m s^{-1}. The dashed line is for $c_s = \bar{u}_0 = 20$ m s^{-1}, and the dotted line is for $c_s = 10$ m s^{-1}. The phase speed of the slowest wave is ~ 3.16 m s^{-1}.

dominance of GWs with westward phase speeds in the upper atmosphere. The double easterly wind reversal above 100 km leads to an enhanced dissipation of the westward traveling waves, and to the strong momentum deposition at these heights. However, the distribution of $|c - \bar{u}|$ does not favor the vertical propagation of GWs, which are absorbed rapidly below 130 km. The difference between the linear and nonlinear saturation schemes is significant in the SH where the peak value of the drag computed with β_{lin}^i (above

Figure 6. Comparison of the linear (dotted line) and the nonlinear (solid line) breaking/saturation schemes including total thermospheric dissipation for 40°N, 40°S, and 0°. S1 spectrum approximated by $M = 20$ harmonics is used.

but is crucial for the linear Hodges-Lindzen-type parameterization with β_{lin}^i. Figure 5 presents the distributions of the flux source spectrum for different c_s and $\bar{u}_0$. The solid line shows the "standard" (centered around $c = 0$) form of the spectrum with the following parameters: $c_{max} = 60$ m s^{-1}, $c_s = 0$, $\overline{u'w'}_{max} = 0.00012$ m^2 s^{-2}, $c_w = 45$ m s^{-1}, $\bar{u}_0 = 0$ m s^{-1}, $k_h = 2\pi/200$ km^{-1} and $M = 20$. It will be referred to as "S1".
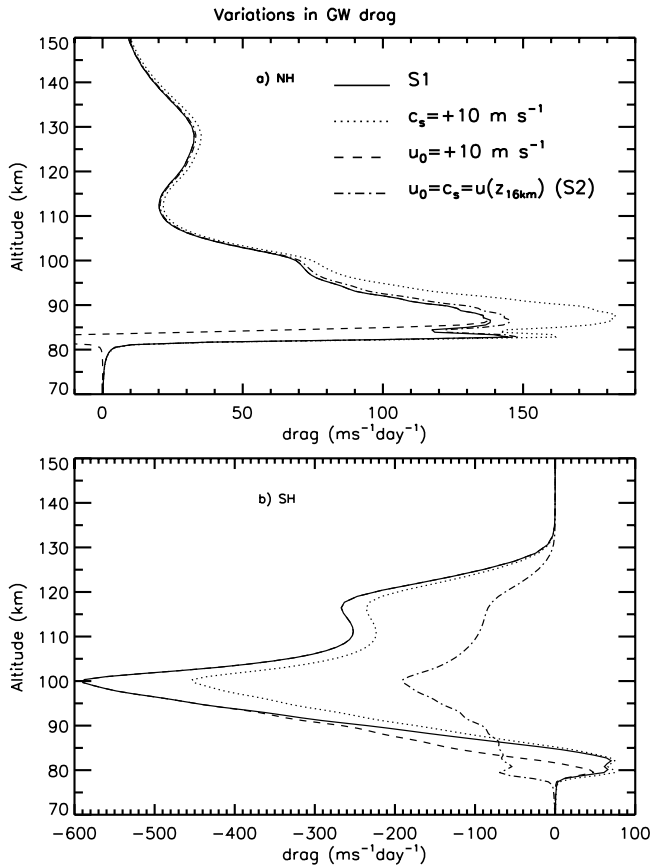
[39] We first compare the β_{lin}^i with β_{non}^i using the prescribed full spectrum S1. GW drag for the three typical wind and temperature distributions is plotted in Figures 6a, 6b, and 6c. The asymmetry of the profiles and the vertical extent of the GWs are caused almost entirely by the background wind, since the temperature and the molecular dissipation differ insignificantly. In the NH, the stratospheric easterlies filter out all westward moving harmonics below 60 km. The eastward directed waves with $c < 30$ m s^{-1} dissipate in the MLT before being absorbed at the critical levels. They are responsible for the maximum drag ~ 150 m s^{-1} d^{-1} near 85 km in the β_{non}^i case. The drag in the linear breaking scheme peaks at 95 km with a larger magnitude (~ 185 m s^{-1} d^{-1}) and 10 km higher than with β_{non}^i. Above 100 km, the surviving waves with $c > 30$ m s^{-1} propagate against the mean wind. Since their intrinsic phase velocities $|c - \bar{u}|$ increase owing to the intensifying easterlies, the effect of the exponential growth of molecular viscosity and neutral-ion collisions is offset to some degree. This enables the GWs to penetrate higher into the thermosphere, to 160 km versus 130 in the Southern Hemisphere (SH) and to 125 km over the equator, and to provide relatively weaker peak drag values of 30 m s^{-1} d^{-1} and 65 m s^{-1} d^{-1} at 130 km by β_{lin}^i and β_{non}^i, respectively.

[40] In the winter hemisphere, westerly winds filter out the eastward traveling waves almost entirely, leading to a

Figure 7. Effects of GW source variation in the northern (NH) and southern (SH) midlatitudes (40°N and 40°S). Parameters of the sources are shown in the plot and described in the text.

1000 m s^{-1} d^{-1}) is much stronger than in the nonlinear case.

[41] The equator is dominated by the westward GW torque similar to the SH. This is mainly due to the common structures of the equatorial and the SH wind profiles above 80 km. There is a competition between eastward and westward momentum deposition in the MLT due to alternating wind reversals in the MLT resulting in two peaks of drag centered at around 95 km and 115 km for β^i_{lin} and β^i_{non}, respectively. Again, β^i_{lin} produces much stronger drag, especially at 115 km, which is at least 5 times larger than for β^i_{non}. Above 120 km, the eastward drag created by large amplitude fast eastward moving waves prevails because the thermospheric easterlies favor the propagation of eastward harmonics. Again, the maximum drag of 40 m s^{-1} d^{-1} is much larger in the linear saturation scheme.

[42] These differences between β^i_{lin} and β^i_{non}, especially above 110 km, are mainly caused by the amount of dissipation imposed on the large phase velocity portion of the spectrum. Note that here, β^i_{lin} does not turn on at all, and wave amplitudes are limited only by β^i_{tot}. On the other hand, β^i_{non} becomes effective lower down, and grows with wave amplitudes. Along with β^i_{tot}, it provides relatively larger damping rates before waves reach significant amplitudes.

This mechanism, as illustrated for single harmonics above, creates smaller drag with smoother vertical profiles.

8. Sensitivity to the Source Spectrum Variations

[43] In the previous sections, we have shown that GW effects can extend into the TI, and that the wave intrinsic phase speed $c_i - \bar{u}$, is the parameter that controls wave propagation. In this section, we outline the sensitivity of the GW drag in the thermosphere to the variations of the source spectrum in the lower atmosphere. Now we use only β^i_{non} in combination with the total "external" dissipation. The results are plotted in Figure 7 for the NH and SH. To allow a clearer intercomparison, the source spectra were scaled to have identical total momentum fluxes. $M = 20$ harmonics were used in the calculations.

[44] The visible hemispheric differences in the GW drag profiles are caused by the wave filtering and modification of the dissipation by the background wind. The Positive shift of c_s allocates larger flux to the harmonics with $c > 0$, and vice versa. For $c_s = 10$ m s^{-1}, this results in an increase of the eastward acceleration in the NH (about 40 m s^{-1} d^{-1} at 85 km) and a decrease of the westward drag in the SH by about 150 m s^{-1} d^{-1} at 100 km. Little changes are produced by the shifted spectrum in the NH and SH above 100 and 120 km, respectively. This can be explained by the increasing importance of thermospheric dissipation. The given variations of the source spectrum do not affect the vertical extent of the GW drag (160 km in the NH, and 130 km in the SH). The long dashed line in Figure 7 shows the drag profiles corresponding to the spectrum with $u_0 = 10$ m s^{-1} and $c_s = 0$. This means that waves with positive phase speeds $0 < c < 10$ m s^{-1} are assigned negative fluxes, and upon dissipation, produce a westward drag. This effect is observed in the SH between 80 and 90 km, where a steep increase of the westward drag is seen. In the NH, the effect is shown by an overall decrease of the eastward drag between 80 and 85 km. It occurs because slow eastward waves (that now have the opposite sign of flux) contribute to the westward acceleration.

[45] One particularly representative and physically plausible spectrum is with $c_s = \bar{u}_0 = \bar{u}(z_0 \approx 16$ km), as shown in Figure 5 with the dashed line for $\bar{u}_0 = 20$ m s^{-1} (hereafter denoted as "S2"). It assigns the maximum GW momentum flux to the harmonics with phase speed equal to the mean wind velocity at the source level, leaving the overall phase velocity distribution unchanged but shifted by the amount $\bar{u}(z_0)$. At the given launch level ($z_0 \approx 16$ km), the wind is westerly in both hemispheres. This creates an asymmetric launch spectrum biased to negative fluxes. The effect of the shift is larger in the SH because $\bar{u}_0 \sim 30$ m s^{-1} is much stronger than in the NH (few m s^{-1}), thus introducing latitudinal variations of the source. As seen in Figure 7, the drag in the NH changes little, while the corresponding profiles in the SH are dramatically different. The westward momentum deposition is noticeable already by around 75 km, and peaks near 80 km at 70 m s^{-1} d^{-1}. The altitude of the global GW drag maximum is unchanged (100 km), but its magnitude is decreased by a factor of three from ~600 to ~200 m s^{-1} d^{-1}. As with S1, the wave drag ceases at around 130 km. A closer examination shows that strong SH westerlies of up to 35 m s^{-1} at the source level cause a marked
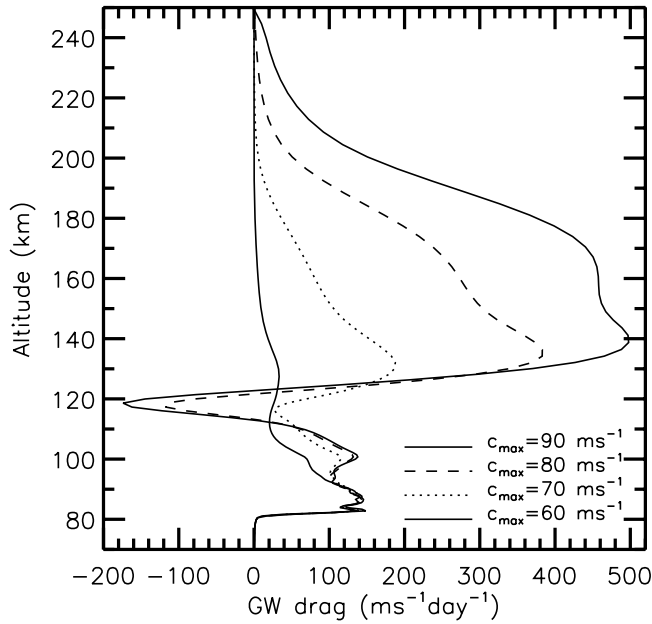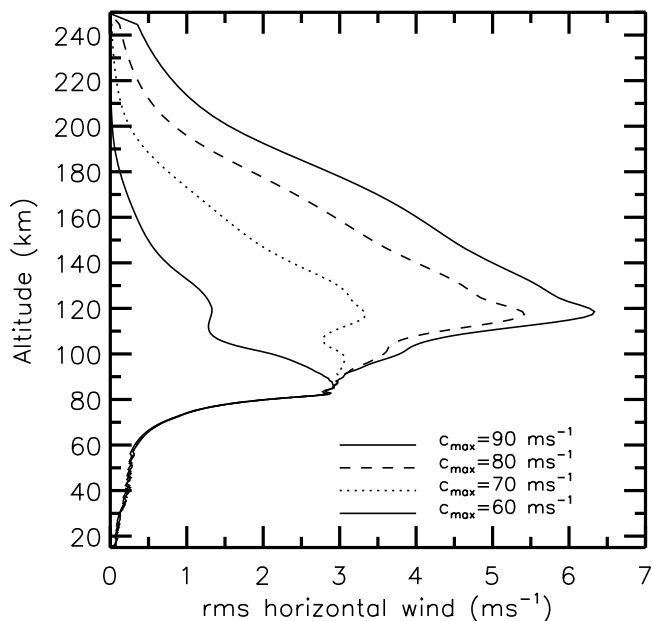
Figure 8. GW drag profiles calculated at 40°N for the S2 source spectrum with the different spectral extent $c_{max} = 60$, 70, 80, and 90 m s^{-1}.

decrease of the momentum flux in the high phase speed portion of $c_I < 0$ waves, thus limiting their impact in the thermosphere. Owing to this shift the middle portion of the spectrum carries on the westward momentum, which causes the local peak of the westward drag near 80 km in the SH.

9. Influence of the High Phase Speed Part of the Spectrum

[46] In this section, we discuss how the inclusion of harmonics with high phase velocity affects the GW drag

in the thermosphere. We use the S2 spectrum and vary the parameter c_{max} that controls spectral extent. Again, in order to have the same total flux at the source level created by all harmonics, $\overline{u'w'}(z_0)$ was normalized as in the calculations in the previous sections. Figure 8 shows the profiles of GW drag computed with four different c_{max}: 60, 70, 80 and 90 m s^{-1}. It is seen that the resulting profiles vary significantly. The difference between the drag for $c_{max} = 60$ and 90 m s^{-1} spectra is about 200 m s^{-1} d^{-1} at 120 km and ~500 m s^{-1} d^{-1} at 140 km. The vertical penetration of the GW drag for the spectrum with $c_{max} = 60$ m s^{-1} is up to 160 km, while it is ~90 km higher for $c_{max} = 90$ m s^{-1}. The extension of c_{max} increases the number of harmonics with higher phase velocities, which are able to survive the filtering by the stratospheric and mesospheric jets and deposit their momentum in the thermosphere. If a particular harmonic is directed against the mean wind, its upward propagation into TI is enhanced also by the offset of the wave dissipation. This is illustrated in Figure 9, which shows the RMS wind fluctuations, i.e., the total wave wind variance σ divided by the number of
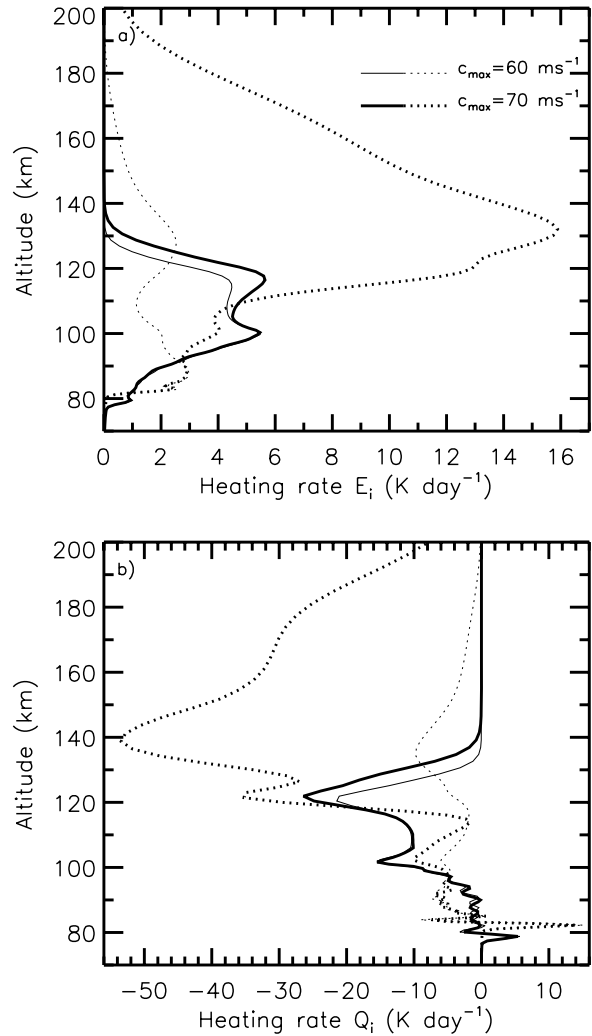
Figure 10. Heating due to dissipating harmonics and (b) differential GW heating, calculated in the NH (dotted lines) and SH (solid lines) for the spectra with $c_{max} = 60$ m s^{-1} (thin line) and $c_{max} = 70$ m s^{-1} (thick line).

Figure 9. The same as in Figure 8, but for the RMS horizontal wind fluctuations.

harmonics in the spectrum. Below $\sim$80 km, the variance grows almost exponentially, being affected only by the easterly jet filtering, and is almost identical in all four cases of c_{max}. Above this height, the variance differs strongly since the number of waves penetrating the thermosphere above the mesospheric westerlies grows with c_{max}. These GW fluctuations with larger amplitude create stronger drag upon dissipation, as Figure 8 depicts.

[47] Saturation of GWs is accompanied by heat deposition due to dissipation of harmonics (E_i) and the downward transport of the mean enthalpy (differential heating Q_i). Figure 10 presents the vertical profiles of both E_i and Q_i calculated according to (6) with the S2 source spectrum described in the previous section. The sensitivity to the source spectrum is demonstrated with c_{max} = 60 and 70 m s^{-1}. In general, the behavior of the heating rates is consistent with that of GW momentum deposition. In the NH, E_i changes significantly (from 2 to 16 K d^{-1} at about 130 km) when c_{max} increases by 10 m s^{-1}. In the SH, both spectra produce $\sim$5 K d^{-1}. The differential cooling in the thermosphere is much stronger. For the spectrum with c_{max} = 70 m s^{-1} it reaches -55 K d^{-1} at 140 km against 10 K d^{-1} for c_{max} = 60 in the NH.

10. Summary and Conclusions

[48] We have presented an extension of a GW drag parameterization into the upper atmosphere suitable for implementation in GCMs extending well into the thermosphere. In addition to the breaking/saturation schemes based on either linear (Hodges-Lindzen) or nonlinear [*Weinstock*, 1982; *Medvedev and Klaassen*, 1995, 2000] closures, this parameterization systematically accounts for realistic wave dissipation due to molecular viscosity, thermal conduction, ion drag and radiative damping in the thermosphere. Dissipation due to molecular viscosity and thermal conductivity was considered, on the basis of a Prandtl number of unity. The parameterization can be applied to broad GW spectra as well as to spectra consisting of individual harmonics.

[49] GW propagation into the thermosphere and the resultant momentum deposition were studied in a series of numerical tests of increasing complexity. The significance of individual dissipative processes was examined in the simplest case for a single harmonic in a windless atmosphere, i.e., in a setup that excludes critical line filtering. In agreement with previous studies, molecular viscosity and thermal conduction are shown to be the dominant dissipative mechanisms, while ion friction and radiative cooling play a secondary role. The linear and nonlinear GW breaking/saturation schemes were tested in conjunction with thermospheric dissipation. We show that the Lindzen-type parameterization produces larger drag than one based on the nonlinear wave interactions [*Weinstock*, 1982; *Medvedev and Klaassen*, 1995, 2000] for both single and multiple harmonic spectra. To reduce the magnitudes of the GW drag computed with parameterizations based on the Hodges-Lindzen breaking criteria, artificial "intermittency" factors are required.

[50] We describe the results of the sensitivity tests for realistic conditions using empirical data from the MSISE-90, HWM, and CHIU models to prescribe the background

propagation and dissipation properties of the neutral atmosphere and ionosphere. The intrinsic phase velocity ($c_i - \bar{u}$), strongly controls wave attenuation via critical line filtering, linear or nonlinear breaking/saturation, and thermospheric dissipation. Our simulations suggest that GW harmonics can experience saturation at multiple heights, therefore parameterizations implying a single breaking level [*Holton*, 1982; *Alexander and Dunkerton*, 1999] may not be able to properly capture the GW momentum deposition in the thermosphere. Dissipation in the TI can significantly alter the occurrence of breaking/saturation events, and thus the associated profiles of drag. Our results illustrate that the effect of thermospheric dissipation is more complex than a simple exponential decay of GW fluxes above certain levels.

[51] This study suggests that GW drag profiles are sensitive to the variations of the source spectrum typically employed in GCMs. The relative distribution of the incident harmonics with respect to the intrinsic phase velocity $c - \bar{u}(z_0)$ (or equivalently to the sign of GW fluxes) at the level of generation, plays a crucial role in shaping the momentum deposition in the middle and upper atmosphere, owing to the selective filtering by the mean wind. Faster GW harmonics are more likely to survive the filtering and dissipation. Therefore, variation associated with the large phase speed portion of the spectrum most strongly impacts the vertical extent of the wave penetration and the shape of the corresponding drag profiles. Under favorable conditions, our simulations suggest that GWs can propagate into, and affect, the circulation of the atmosphere to altitudes as high as 250 km.

References

Akmaev, R. A. (2001), Simulation of large-scale dynamics in the mesosphere and lower thermosphere with the Doppler-spread parameterization of gravity waves: 1. Implementation and zonal mean climatologies, *J. Geophys. Res.*, *106*, 1193–1204.

Alexander, M. J., and T. J. Dunkerton (1999), A spectral parameterization of mean-flow forcing due to breaking gravity waves, *J. Atmos. Sci.*, *56*, 4167–4182.

Allen, S. J., and R. A. Vincent (1995), Gravity wave activity in the lower atmosphere: Seasonal and latitudinal variations, *J. Geophys. Res.*, *100*, 1327–1350.

Banks, P. M., and G. Kockarts (1973), *Aeronomy Part B*, 355 pp., Elsevier, New York.

Becker, E. (2004), Direct heating rates associated with gravity wave saturation, *J. Atmos. Sol. Terr. Phys.*, *66*, 683–696.

Ching, B. K., and Y. T. Chiu (1973), A phenomenological model of global ionospheric electron density in the E-, F1-, and F2-regions, *J. Atmos. Terr. Phys.*, *35*, 1615–1630.

Chiu, Y. T. (1975), An improved phenomenological model of ionospheric density, *J. Atmos. Terr. Phys.*, *37*, 1563–1570.

Djuth, F. T., M. P. Sulzer, S. A. Gonzales, J. D. Mathews, J. H. Elder, and R. L. Walterscheid (2004), A continuum of gravity waves in the Arecibo thermosphere?, *Geophys. Res. Lett.*, *31*, L16801, doi:10.1029/2003GL019376.

Espy, P. J., R. E. Hibbins, G. R. Swenson, J. Tang, M. J. Taylor, D. M. Riggin, and D. C. Fritts (2006), Regional variations of mesospheric gravity-wave-momentum flux over Antarctica, *Ann. Geophys.*, *24*, 81–88.

Fomichev, V. I., W. E. Ward, S. R. Beagley, C. McLandress, J. C. McConnell, N. A. McFarlane, and T. G. Shepherd (2002), Extended Canadian Middle Atmosphere model: Zonal-mean climatology and physical parameterizations, *J. Geophys. Res.*, *107*(D10), 4087, doi:10.1029/2001JD000479.

Fritts, D. C., and M. J. Alexander (2003), Gravity wave dynamics and effects in the middle atmosphere, *Rev. Geophys.*, *41*(1), 1003, doi:10.1029/2001RG000106.

Fritts, D. C., and W. Lu (1993), Spectral estimates of gravity wave energy and momentum flux. Part II: Parameterization of wave forcing and variability, *J. Atmos. Sci.*, *50*, 3695–3713.

Garcia, R. R., D. R. Marsh, D. E. Kinnison, B. A. Boville, and F. Sassi (2007), Simulations of secular trends in the middle atmosphere, *J. Geophys. Res.*, *112*, D09301, doi:10.1029/2006JD007485.

Gavrilov, N. M. (1990), Parameterization of acceleration and heat flux divergence by internal gravity waves in the middle atmosphere, *J. Atmos. Terr. Phys.*, *9*, 707–713.

Gossard, E. E., and W. H. Hooke (1975), *Waves in the Atmosphere*, 243 pp., Elsevier, New York.

Hedin, A. E. (1991), Extension of the MSIS thermosphere model into the middle and lower atmosphere, *J. Geophys. Res.*, *96*, 1159–1172.

Hedin, A. E., et al. (1996), Empirical wind model for the upper, middle and lower atmosphere, *J. Atmos. Terr. Phys.*, *58*, 1421–1447.

Hickey, M. P., and K. D. Cole (1988), A numerical model for gravity wave dissipation in the thermosphere, *J. Atmos. Terr. Phys.*, *50*, 689–697.

Hines, C. O. (1960), Internal gravity waves at ionospheric heights, *Can. J. Phys.*, *38*, 1441–1481.

Hines, C. O. (1997), Doppler-spread parameterization of gravity wave momentum deposition in the middle atmosphere. Part 1: Basic formulation, *J. Atmos. Sol. Terr. Phys.*, *59*, 371–386.

Hines, C. O., and W. H. Hooke (1970), Discussion of ionization effects on the propagation of acoustic-gravity waves in the ionosphere, *J. Geophys. Res.*, *75*, 2563–2568.

Hodges, R. R. (1967), Generation of turbulence in the upper atmosphere by internal gravity waves, *J. Geophys. Res.*, *72*, 3455–3458.

Holton, J. R. (1982), The role of gravity wave induced drag and diffusion in the momentum budget of the mesosphere, *J. Atmos. Sci.*, *39*, 791–799.

Johnson, M. H., and E. O. Hulbert (1950), Diffusion in the ionosphere, *Phys. Rev.*, *79*, 802–807.

Kazimirovsky, E., M. Herraiz, and A. D. L. B. Morena (2003), Effects on the ionosphere due to phenomena occurring below it, *Surv. Geophys.*, *24*, 139–184.

Klostermeyer, J. (1972), Influence of viscosity, thermal conduction, and ion drag on the propagation of atmospheric gravity waves in the thermosphere, *Z. Geophys.*, *38*, 881–890.

Lindzen, R. S. (1981), Turbulence and stress owing to gravity waves and tidal breakdown, *J. Geophys. Res.*, *86*, 9707–9714.

Matsuno, T. (1982), A quasi one-dimensional model of the middle atmosphere circulation interacting with internal gravity waves, *J. Meteorol. Soc. Jpn.*, *60*, 215–226.

Medvedev, A. S., and G. P. Klaassen (1995), Vertical evolution of gravity wave spectra and the parameterization of associated wave drag, *J. Geophys. Res.*, *100*, 25,841–25,853.

Medvedev, A. S., and G. P. Klaassen (2000), Parameterization of gravity wave momentum deposition based on nonlinear wave interactions: Basic formulation and sensitivity tests, *J. Atmos. Sol. Terr. Phys.*, *62*, 1015–1033.

Medvedev, A. S., and G. P. Klaassen (2003), Thermal effects of saturating gravity waves in the atmosphere, *J. Geophys. Res.*, *108*(D2), 4040, doi:10.1029/2002JD002504.

Meyer, C. K. (1999a), Gravity wave interactions with the diurnal propagating tide, *J. Geophys. Res.*, *104*, 4223–4239.

Meyer, C. K. (1999b), Gravity wave interactions with mesospheric planetary waves: A mechanism for penetration into the thermosphere-ionosphere system, *J. Geophys. Res.*, *104*, 28,181–28,196.

Miyoshi, Y., and H. Fujiwara (2008), Gravity waves in the thermosphere simulated by a general circulation model, *J. Geophys. Res.*, *113*, D01101, doi:10.1029/2007JD008874.

Nakamura, T., T. Tsuda, R. Maekawa, M. Tsutsumi, K. Shiokawa, and T. Ogawa (2001), Seasonal variation of gravity waves with various temporal and horizontal scales in the MLT region observed with radar and airglow imaging, *Adv. Space Res.*, *27*, 1737–1742.

Oliver, W. L., Y. Otsuka, M. Sato, T. Takami, and S. Fukao (1997), A climatology of F region gravity wave propagation over the middle and upper atmosphere radar, *J. Geophys. Res.*, *102*, 14,499–14,512.

Pitteway, M. L. V., and C. O. Hines (1963), The viscous damping of atmospheric gravity waves, *Can. J. Phys.*, *41*, 1935–1948.

Rishbeth, H. (1979), Ion drag effects in the thermosphere, *J. Atmos. Terr. Phys.*, *41*, 885–894.

Schmidt, H., G. P. Brasseur, M. Charron, E. Manzini, M. A. Giorgetta, T. Diehl, V. I. Fomichev, D. Kinnison, D. Marsh, and S. Walters (2006), The HAMMONIA Chemistry Climate Model: Sensitivity of the mesopause region to the 11-year solar cycle and CO_2 Doubling, *J. Clim.*, *19*, 3903–3931.

Vadas, S. L. (2007), Horizontal and vertical propagation of gravity waves in the thermosphere from lower atmospheric and thermospheric sources, *J. Geophys. Res.*, *112*, A06305, doi:10.1029/2006JA011845.

Vadas, S. L., and D. C. Fritts (2005), Thermospheric responses to gravity waves: Influences of increasing viscosity and thermal diffusivity, *J. Geophys. Res.*, *110*, D15103, doi:10.1029/2004JD005574.

Vadas, S. L., D. C. Fritts, and M. J. Alexander (2003), Mechanism for the generation of secondary waves in wave breaking regions, *J. Atmos. Sci.*, *60*, 194–214.

Warner, C. D., and M. E. McIntyre (2001), An ultrasimple spectral parameterization for non-orographic gravity waves, *J. Atmos. Sci.*, *58*, 1837–1857.

Weinstock, J. (1976), Nonlinear theory of acoustic-gravity waves: 1. Saturation and enhanced diffusion, *J. Geophys. Res.*, *81*, 633–652.

Weinstock, J. (1982), Nonlinear theory of gravity waves: Momentum deposition, generalized Rayleigh friction, and diffusion, *J. Atmos. Sci.*, *39*, 1698–1710.

Weinstock, J. (1990), Saturated and unsaturated spectra of gravity waves and scale-dependent diffusion, *J. Atmos. Sci.*, *47*, 2211–2225.

Williams, P. J. S., N. J. Mitchell, A. G. Beard, V. St. C. Howells, and H. G. Muller (1999), The coupling of planetary waves, tides and gravity waves in the mesosphere and lower thermosphere, *Adv. Space Res.*, *24*, 1571–1576.

Wu, D. L., and J. W. Waters (1996), Satellite observations of atmospheric variances: A possible indication of gravity waves, *Geophys. Res. Lett.*, *23*, 3631–3634.

————————————

A. D. Aylward and E. Yiğit, Department of Physics and Astronomy, University College London, Gower Street, London WC1E 6BT, UK. (alan@apl.ucl.ac.uk; erdal@apl.ucl.ac.uk)

A. S. Medvedev, Max Planck Institute for Solar System Research, Katlenburg-Lindau D-37191, Germany. (medvedev@mps.mpg.de)